Published as: Jariyavidyanont, K., Williams, J. L., Rhoades, A. M., Kühnert, I., Focke, W. and Androsch, R. (2018), Crystallization of polyamide 11 during injection molding. Polym Eng Sci, 58: 1053-1061. https://doi.org/10.1002/pen.24665

Crystallization of polyamide 11 during injection molding

Katalee Jariyavidyanont [1*], Jason L. Williams [2], Alicyn M. Rhoades [2], Ines Kühnert [3], Walter Focke [4], René Androsch [1*]

[1] Interdisciplinary Center for Transfer-Oriented Research in Natural Sciences, Martin Luther University Halle-Wittenberg, 06099 Halle/Saale, Germany

[2] School of Engineering, Penn State Behrend, 4701 College Drive, Erie, PA 16563, United States

[3] Institute of Polymer Materials, Department of Processing. Leibniz-Institute fuer Polymerforschung Dresden e. V., Hohe Str. 6, 01069 Dresden, Germany

[4] Institute of Applied Materials, Department of Chemical Engineering, University of Pretoria, Private Bag X20, Hatfield 0028, Pretoria, South Africa

* Corresponding Authors:

K. Jariyavidyanont (katalee.jariyavidyanont@iw.uni-halle.de)
R. Androsch (rene.androsch@iw.uni-halle.de)

Abstract

The semicrystalline morphology of injection moldings of polyamide 11 (PA 11) prepared using mold temperatures of 25, 50, and 80 °C was investigated. Regardless the mold temperature, position-resolved X-ray diffraction (XRD) and polarized-light optical microscopy (POM) revealed presence of poor/imperfect α-crystals with an almost hexagonal arrangement of molecular stems in a non-spherulitic superstructure in the skin, and formation of α-crystals and spherulites in the core. With increasing mold temperature, the thickness of the skin layer decreased, and the perfection of α-crystals as well as the spherulite size in the core increased. The experimental observations are discussed in terms of predicted crystallization temperatures, with the prediction based on cooling-rate simulations for the various parts of the injection moldings using Moldflow® and analysis of crystallization of the relaxed melt using fast scanning chip calorimetry, XRD, and POM. It is shown that the structure gradient in PA 11 injection moldings can be forecast without considering the effects of shear for this particular polymer.

Introduction

Polyamide 11 (PA 11) is a crystallizable bio-based polymer generally used for high-performance engineering applications as it has excellent resistance to chemicals and solvents, good thermal stability, and impact resistance at low temperature, as well as rather low moisture uptake compared to other polyamides [1]. With respect to processing by injection molding, such applications include fittings, connectors, gears, syringes, cable ties, or phone housings. Similar to other crystallizable polymers, the physical and mechanical properties of PA 11 are influenced by the semicrystalline morphology including the fraction and structure of crystals, their size, shape and perfection, and their organization in a higher-order superstructure, which all can be controlled by the condition of crystallization/processing [2–5]. Regarding the crystal structure, it is known that PA 11 is polymorphic, that is, different crystal polymorphs may develop as a function of the crystallization conditions [6–16]. As is illustrated in Figure 1, melt crystallization at slow cooling (right pathway) occurs around 150–160 °C and typically leads to formation of pseudohexagonal δ-crystals which on further cooling reversibly convert at the Brill transition temperature into triclinic α-crystals [15]; the crystallinity may then reach values of 30 %. At high supercooling of the melt, as has first been discovered by quenching the melt into ice-water, formation of a pseudohexagonal, less ordered, smectic-like δ'-mesophase occurs [16] (left path). The δ'-phase is metastable at the temperature of formation and at lower temperatures, and it irreversibly transforms at elevated temperature into the δ/α-structure [13]. There exist reports about further polymorphs of PA 11 which may develop upon solution-crystallization [17, 18], or about crystallization in presence of pressure [8]. Regarding the latter it was found that crystallization under pressure can produce crystals of different thermal stability though not necessarily different crystal structure than typically obtained on crystallization at atmospheric pressure. We are not aware about studies of shear-induced crystallization of PA 11.

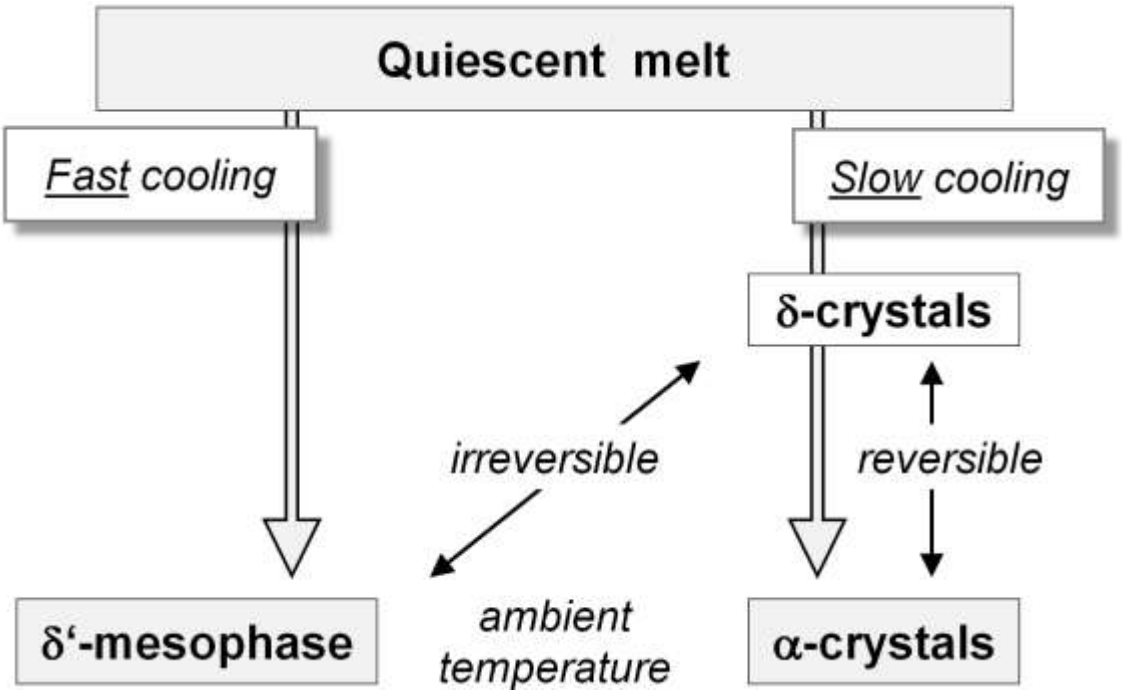

Figure 1: Cooling-rate controlled crystal polymorphism in PA 11. The right and left crystallization pathways represent crystallization at slow and fast cooling, respectively.

To obtain information about the non-isothermal and isothermal crystallization kinetics, specific experiments have been performed using fast scanning chip calorimetry [19, 20], permitting analysis of crystallization of the quiescent melt at conditions relevant in processing, that is, on cooling at rates up to 1000 K s^{-1} and at high supercooling of the melt [21–23]. It was found that the critical cooling rate to suppress crystallization is around 600 K s^{-1} in case of neat PA 11, and that on cooling at rates higher than about 100 K s^{-1} formation of δ-crystals at low supercooling is incomplete. Incomplete high-temperature crystallization allows then the development of δ'-mesophase at high supercooling, close to the glass transition temperature T_g. The observation of formation of δ-crystals and δ'-mesophase on cooling at different rates, and occurring at different crystallization temperatures, is paralleled by the detection of a bimodal temperature-dependence of the crystallization rate which similar as in other polymers is associated to a change from heterogeneous nucleation at low melt-supercooling to homogeneous nucleation at high melt-supercooling [24–26]. A correlation between the crystallization temperature, the mechanism of crystal nucleation and the crystal polymorphism has been reported recently for a specific PA 11 grade [14]; note that the critical supercooling at which pre-dominance of homogeneous nucleation is observed depends on the specific PA 11 grade investigated, that is, on the presence of possible heterogeneous nucleation sites.

Injection molding, that is, injecting the polymer melt into a cavity, is a common polymer-processing technology due to its efficiency to produce both simple and intricate parts with high production output. During injection molding, the semicrystalline microstructure of the polymer forms under shear and thermal gradients that result in the development of variable morphologies between the outer skin and inner core of the molded sample. The resulting, often stratified microstructure imparts subsequent implications on the mechanical property profile. As a net result of the effects of shear, pressure, and thermal fields during injection molding, often skin/core morphologies with a layer-like or gradient structure regarding the orientation of macromolecules and crystals, the crystallinity, or the crystalline-amorphous superstructure develop [27–30]. It is well-established that variation of the molding conditions such as melt temperature, injection-pressure/time, or mold temperature affects the skin/core morphology [29–36]. However, to the best of our knowledge, specific reports about the skin/core structure of injection moldings based on PA 11 are not available, which is in contrast to numerous studies performed on different polyamides (PA 6 and PA 66) [28, 29, 33–36]. For example, in those systems it has been proven that the skin was featureless in the optical microscope while the core showed spherulites that increased in size with increasing distance from the mold-wall. Furthermore, it was shown that the thickness of the non-spherulitic skin layer decreased with increasing temperature of both the mold and melt [29, 34, 35]. Because of the different cooling rate in the various parts of the molding, the crystalline component in the skin was rich in mesophase while the core mainly contained crystals [33, 34]. In more detail, in a study of the structure and properties of PA 66 injection moldings it was found that the cooling conditions are in particular of importance in thin-wall injection moldings and that slow cooling, enforced by increased mold temperatures, reduces or inhibits the development of a surface layer, allows a more homogeneous morphology, and also affects the crystallinity which increases with a reduced cooling rate. The latter has been analyzed by infrared spectroscopy as a function of the position in the moldings, which in addition to the effect of the mold temperature/cooling rate also allowed identification of the effect of variable shear along the cross section on the crystallinity [29]. The observation of an increased fraction of mesophase a result of faster cooling (evident in surface-near regions, or when using low mold-temperatures) is expected to have implications on the local properties as it was suggested that PA 6 containing mesophase has a distinctly lower Young's modulus and hardness than PA 6 containing similar amount of α-crystals [37, 38]. Due to the lack of knowledge regarding crystallization of PA 11 during injection molding, in the present

study PA 11 injection moldings were prepared using molds of different temperatures to facilitate different heat transfer scenarios. Using known molding parameters, simulation was used to estimate cooling rates through the part as a function of time. These location-specific cooling rates provide a link to the resulting semicrystalline morphology, evaluated by X-ray diffraction (XRD), differential scanning calorimetry (DSC), and polarized-light optical microscopy (POM).

Experimental

Materials and processing

High viscosity PA 11 containing less than 7.5 % BBSA plasticizer, controlled by blending neat BESNO TL and BESNO P20 TL grades from Atofina, was used in this study [1], with the blend prepared by melt-compounding using a Nanjing Ouli Extrusion Machinery Co., Ltd. Model TE-30/600-11-40 co-rotating twin-screw extruder (screw diameter = 30 mm, L/D = 40) with a barrel temperature of 200 °C and screw speed of 200 rpm. Prior to compounding, the materials were dried at 90 °C for more than 12 h. The extruded pellets were dried overnight at 85 °C and then injection molded to standard dumbbell-shaped tensile specimens with a thickness of 2 mm (DIN EN ISO 527-2-1BA) using a BOY 22 A HV machine with a screw diameter of 18 mm. A machine-set melt temperature of 250 °C was used for molding. The maximum volumetric flow rate was set to 10 cm^3 s^{-1} and the maximum holding pressure was 85 bar for a time period of 5.5 s. The cooling time was 15, 17, and 22 s for the molding experiments using mold temperatures of 25, 50, and 80 °C, respectively. Relevant processing parameters are summarized in Table 1.

Table 1. Injection molding parameters.

Parameters	**Unit**			
mold temperature	°C	25	50	80
temperature profile for melting	°C	nozzle 250		
		250		
		240		
		220		
		hopper area 50		
injection profile (speed; way)	mm/s; mm	40; 21		
		37.5; 7		
		35; 6.2		
switching from injection to holding by	-	screw position		
holding-pressure time	s	5 ; 5		
holding-pressure maximal	bar	85		
holding-pressure profile	s; bar	3; 85		
		4; 45		
		5; 15		
		5.5; 0		
cooling time	s	15	17	22
total cooling time (packing time + cooling time)	s	20.5	22.5	27.5
cycle-time average	s	30	31	36
screw diameter	mm	18		

Cooling-rate simulation

The Autodesk®Moldflow 2016 software was used to simulate the cooling rates of the actual physical samples during the injection molding. The simulation was conducted to evaluate the temperature-time profile at specific locations of the samples, in order to estimate the cooling-rate condition at the selected regions for structural analyses by XRD, DSC, and POM. Figure 2 shows the CAD 3D model of the molded specimen including the mold geometry of the sprue, runner, gate, and part, and it was imported into the modeling software to generate a 3D mesh geometry which is consisted of 4-node tetrahedral elements. The mesh geometry was then refined to create 10 layers of elements through the thickness of the model, illustrated in the top part of Figure 2, in order to accommodate and depict the thermal layer gradient through the thickness of the model. Then, a mesh bias factor was applied to create a denser mesh near the skin of the part and a coarser mesh in the core of the part. The mesh bias generated thinner elements of 50 µm close to the surface of the part and thicker elements of 850 µm near the core of the part. Once the mesh was completed, measurement nodes were located at the center cross section of the molding. These nodes corresponded to the sample locations used in the actual physical

evaluation of molded parts at distances of 50, 200, 700, and 1000 µm (white circles) from the skin in direction parallel to the normal of the specimen. The specimen normal direction (ND) as well as the machine direction (MD) (direction of flow) and transverse direction (TD) are indicated with the coordinate system in the top right corner of the model. To generate the practical flow of the melt, material data of Rilsan® BESNO P20 D from the standard Moldflow database were imported. An interpolated specific heat capacity that varied between 1.71 J g^{-1} K^{-1} at 23 °C and 2.73 J g^{-1} K^{-1} at 250 °C was used. The thermal conductivity in the dataset was 0.28 W m^{-1} K^{-1}.

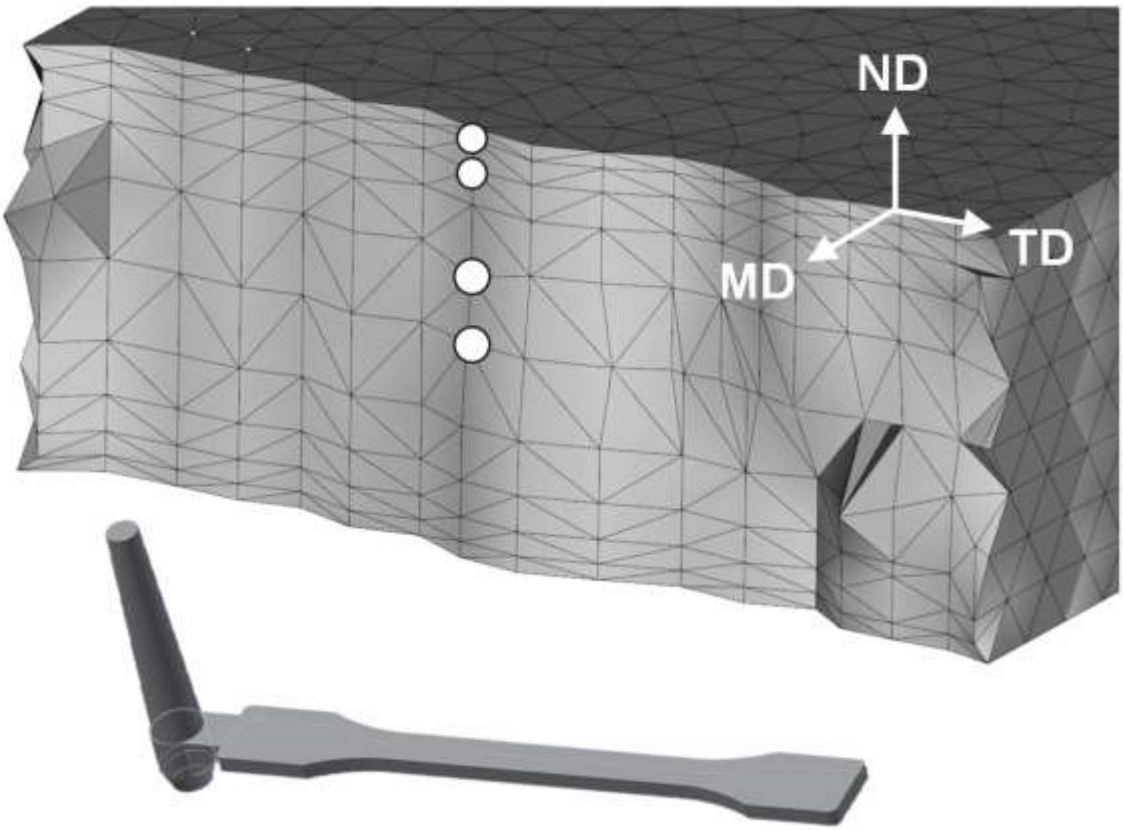

Figure 2: CAD 3D model of the molded specimen imported to the Moldflow software (bottom, left) and locations assigned for the simulation (top), indicated by white spots at distances of 50, 200, 700, and 1000 µm from the surface (from top to bottom, respectively).

Once the model was constructed and material selected, actual process settings were replicated in the software. The setting parameters showed in Table 1 were used for each of the simulation runs. The heat transfer coefficient between the melt and mold wall was 5000 W m^{-2} K^{-1} during the filling phase and 2500 W m^{-2} K^{-1} during the packing phase, to represent the reduced heat transfer due to lower contact pressure. The time step defaults were used and are determined by percentage of part volume. The maximum percent change

in volumetric fill was 2 % per time step. During the packing and cooling phases, a maximum time step of 1 s was used.

Polarized-light optical microscopy (POM)

Sections with a thickness of 50 µm were prepared using a SLEE rotary microtome CUT 4062 equipped with a tungsten carbide knife and then subsequently embedded in immersion oil between two cover slips. The location of sampling in the injection molded test bar is shown in Figure 3, illustrating that the sections were taken parallel to the TD-ND plane. The microstructure of the specimens was then observed by a Motic BA410 optical microscope in transmission mode using crossed polarizers and with the images captured *via* a Moticam 2300 CCD camera.

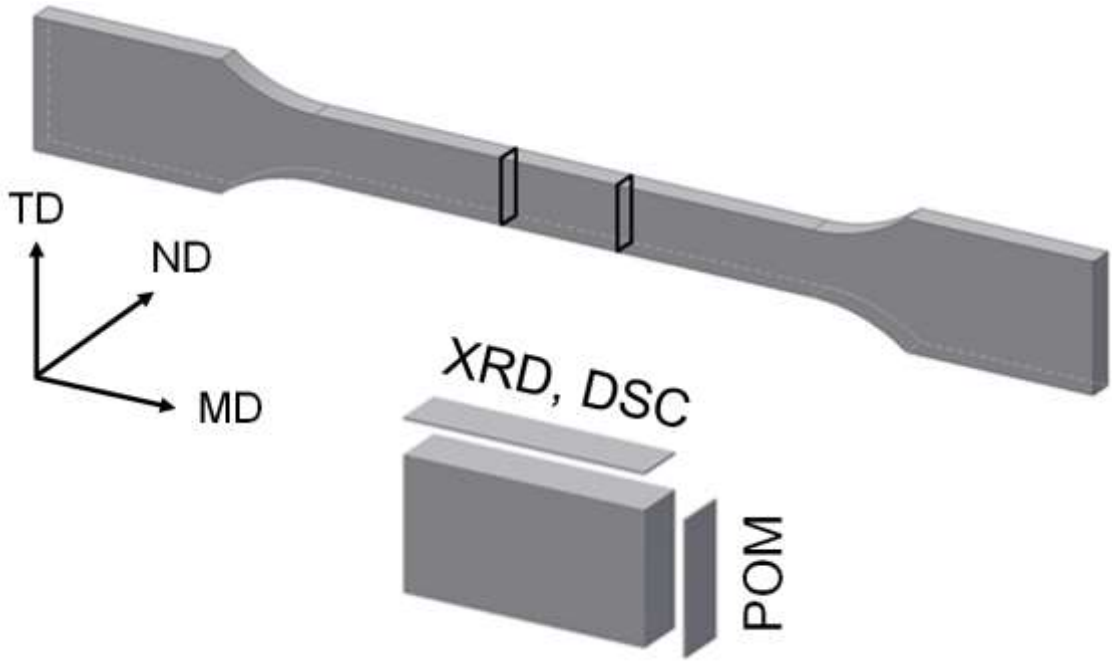

Figure 3: Sketch of the injection-molded test bar, and location/sampling of specimens for POM, DSC, and XRD analyses of the microstructure.

X-ray diffraction (XRD)

Sampling of specimens for XRD analysis of the microstructure of the injection molding is shown in Figure 3. As such, sections were prepared parallel to the ND-MD direction of the molding. In order to identify a structural gradient from skin to core, sectioning began at the outermost skin with an increment of 50 µm for the first 5 slices towards the center region, which then is followed with a slightly increased increment of 70 µm. The X-ray structure of the section was then investigated in transmission mode using a Rigaku DMAX-Rapid II diffractometer equipped with a Cu X-ray tube and a graphite monochromator. The diameter of the circular beam was 800 µm and the exposure time was 180 s. The scattered

X-ray intensity was recorded using a curved image plate detector. Note that we consider the analysis of the samples of slightly different thickness (50 versus 70 µm) uncritical regarding drawing conclusions about the phase structure, in particular since the diameter of the X-ray beam is more than 10× larger than the sample thickness.

Differential scanning calorimetry (DSC)

DSC was employed for analysis of the crystallinity in the skin layer and the central part of the injection moldings, taken at distances of 50 and 700 µm from the surface, respectively. In order to assess the structure at the surface, sections with a thickness of 50 µm were cut parallel to the ND-MD plane of the molding (see Figure 3) and placed into 20 µL aluminum pans. In order to avoid uncertainties due to specimen-sampling, samples from the core region were prepared similarly, that is, using a microtome and collection of section with a thickness of 50 µm. The sample mass was around 1 mg. A heat-flux DSC 1 from Mettler-Toledo in combination with a TC 100 intracooler from Huber was used, with the furnace purged with nitrogen gas at a flow rate of 60 mL min^{-1}. The instrument was calibrated based on the temperature and enthalpy of melting using an indium standard. The crystallinity in the skin and core of the PA 11 injection moldings was then estimated from the enthalpy of melting in the first heating scan recorded at a rate of 10 K min^{-1}, using a value of the bulk enthalpy of melting of 189 J g^{-1} [39].

Results and discussion

Figure 4 shows cooling rates during injection molding of PA 11 at distances of 50 µm (squares), 200 µm (circles), 700 µm (triangles), and 1000 µm (diamond symbols) from the mold-wall to the core region as a function of the temperature of the melt. With the top, center, and bottom plots are shown simulations for mold temperatures of 25, 50, and 80°C, respectively. The star symbols in each plot represent peak-temperatures of crystallization, which were measured as a function of cooling rate in an independent study of the crystallization behavior of the quiescent melt [20]. With the vertical gray lines are indicated in each plot the temperature of the melt (250 °C) and of the temperature of the mold (25, 50, and 80 °C, from top to bottom, respectively).

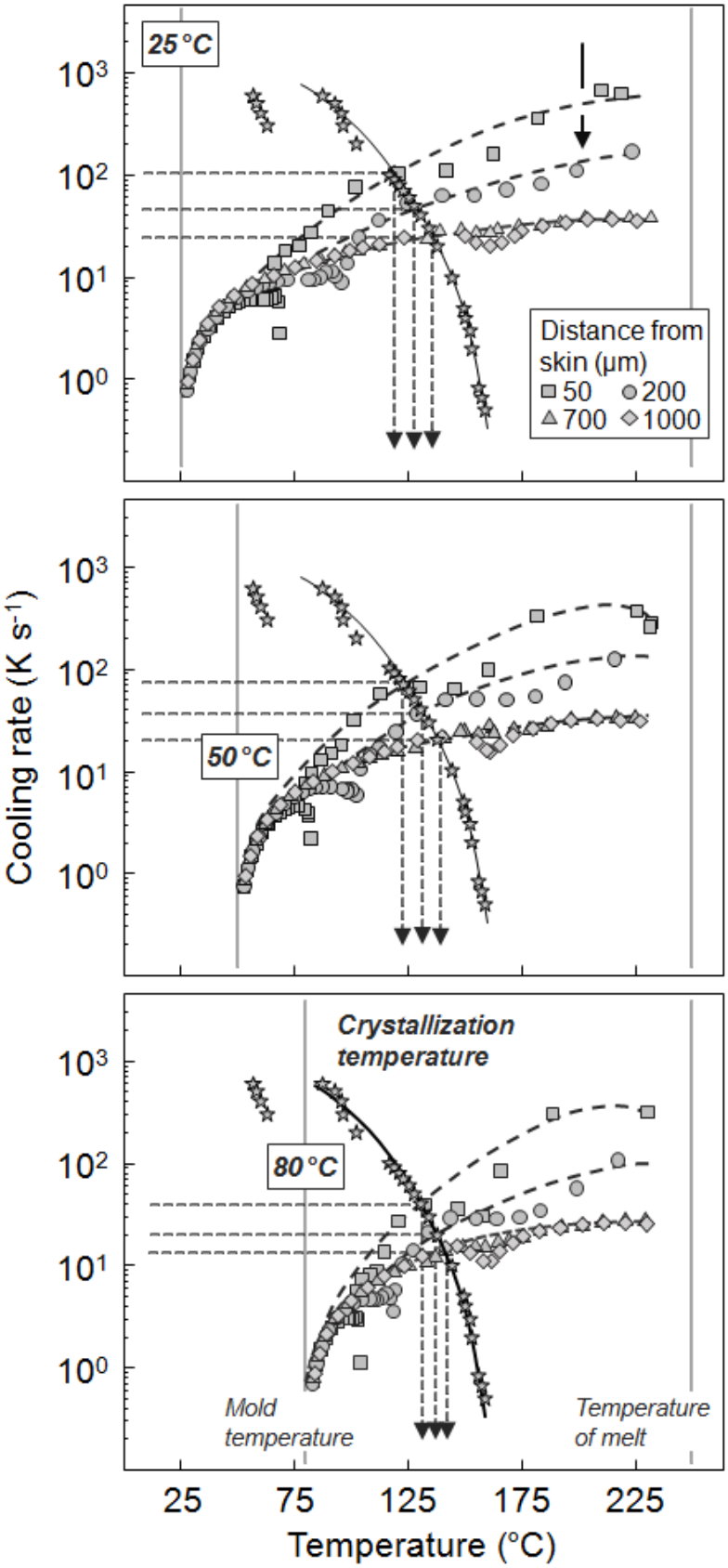

Figure 4: Cooling rate during injection molding of PA 11 at different distance from the mold-wall as a function of the temperature of the melt. With the top, center, and bottom plots are shown simulations for mold temperatures of 25, 50, and 80 °C, respectively. The star symbols in each plot represent peak-temperatures of crystallization of PA 11, which were measured as a function of cooling rate in an independent study of the crystallization behavior of the quiescent melt. FSC data/crystallization temperatures were adapted with kind permission from Springer [20].

Regarding the temperature-dependence of the cooling rate, molding simulation unsurprisingly predicted that the cooling rate decreases with decreasing temperature of the component/molding. More important, the data reveal that with increasing distance from the surface of the injection molding the cooling rate decreases, with the differences most distinct at high temperatures. When the melt is injected into the mold, cooling of the outermost skin at a distance of 50 µm below the surface occurs at a rate of few hundred K s^{-1} at temperature around 200 °C, with the highest cooling-rate value of about 700 K s^{-1} predicted for the setup with a mold temperature of 25 °C; in case of mold temperatures of 50 and 80 °C, the maximum cooling rate at this location is around 400 and 300 K s^{-1}, respectively. For the sample injected into the mold with a temperature of 25 °C (top plot), the cooling rate at about 200 °C decreases from 600 K s^{-1} at a distance of 50 µm below the surface to values of about 100 and 40 K s^{-1} at distances of 200 and 700 µm below the surface (see vertical black arrow in the top plot). In case of mold temperatures of 50 °C (center plot) and 80 °C (bottom plot) the maximum cooling rate at the various distances from the surface of the molding is slightly lower than in case of a mold temperature of 25 °C. With decreasing temperature, however, the cooling-rate differences between skin and core are less pronounced, as all curves in the various plots merge at temperatures close to the mold temperature.

To predict the temperature of crystallization in the injection moldings at the selected distances from the surface, the cooling-rate dependence of crystallization temperatures of PA 11 is inserted in all plots (star symbols), as determined in a separate study [20]. Accordingly, the crystallization temperature of PA 11 decreases with increasing cooling rate from about 160 °C on cooling slower than 1 K s^{-1} to around 80 °C on fast cooling at a rate of few hundred K s^{-1}. If the cooling rate is higher than about 600 K s^{-1} then formation of α/δ-crystals of PA 11 is suppressed. As a result of incomplete high-temperature crystallization, in a rather narrow cooling-rate range between about 200 and 600 K s^{-1} there is observed formation of δ'-mesophase at around 50 °C *via* a homogeneous crystal-nucleation process [14, 22–24]. Inspection of both data sets, cooling rate as a function of temperature and crystallization temperature as a function of cooling rate, provides information about the expected temperature of crystallization in the moldings, given by their intersections.

For example, if the skin of the injection molding prepared using a mold temperature of 25°C (top plot) is cooled at rates higher than about 100 K s^{-1}, which is valid for temperatures higher than about 120 °C then crystallization cannot occur since it is known that crystallization at these high rates would only occur at temperatures lower than about 120 °C (see star-symbols); crystallization is expected when both curves intersect, in this case at about 120 °C when cooling occurs at a rate of around 100 K s^{-1}. With the dashed horizontal lines and vertical arrows are indicated in each plot the cooling rate and temperature at which crystallization occurs in the various layers of the injection moldings, respectively. Without going into detail, crystallization in the injection moldings prepared using mold temperatures of 25, 50, and 80 °C occurs at temperatures between 117 and 135 °C, 121 and 139 °C, and 131 and 142 °C, respectively, with the lower and higher value valid for the skin and core regions of the moldings, respectively. Obviously, the difference between the crystallization temperatures at the skin and in the core is only about 10 K if the mold temperature is 80 °C and about 20 K if the mold temperature is 25 °C.

Figure 5 shows three sets of XRD patterns of PA 11 which was injection molded using different mold temperatures of 25 °C (top), 50 °C (center), and 80 °C (bottom). The various curves in the different data sets were obtained on specimens taken at different distance between 50 µm and 700 µm from the surface, with the sampling illustrated in Figure 3. Regardless the mold temperature, the XRD patterns of the skin of the injection moldings show two strongly overlapping peaks at scattering angles 2θ of about 20.5 and 22 deg which are assigned to the (100) and (010)/(110) lattice planes of triclinic α-crystals [40]. These α-crystals possess high degree of imperfection, as it is concluded from the closeness of the observed scattering peaks. The angular distance between the 100 and 010/110 peaks is a measure of the anisotropy of the unit cell in cross-chain direction, and with that of the degree of the planar alignment of hydrogen bonds between molecular stems [41, 42]; note that in case of a pseudo-hexagonal lattice the observed equatorial peaks would have been merged as it is evident in case of the δ'-mesophase. With increasing distance from the surface of the injection moldings, the perfection of the detected α-crystals improves, which is indicated by the change of the angular position of the 100 and 010/110 scattering peaks (see dashed lines in the bottom set of curves).

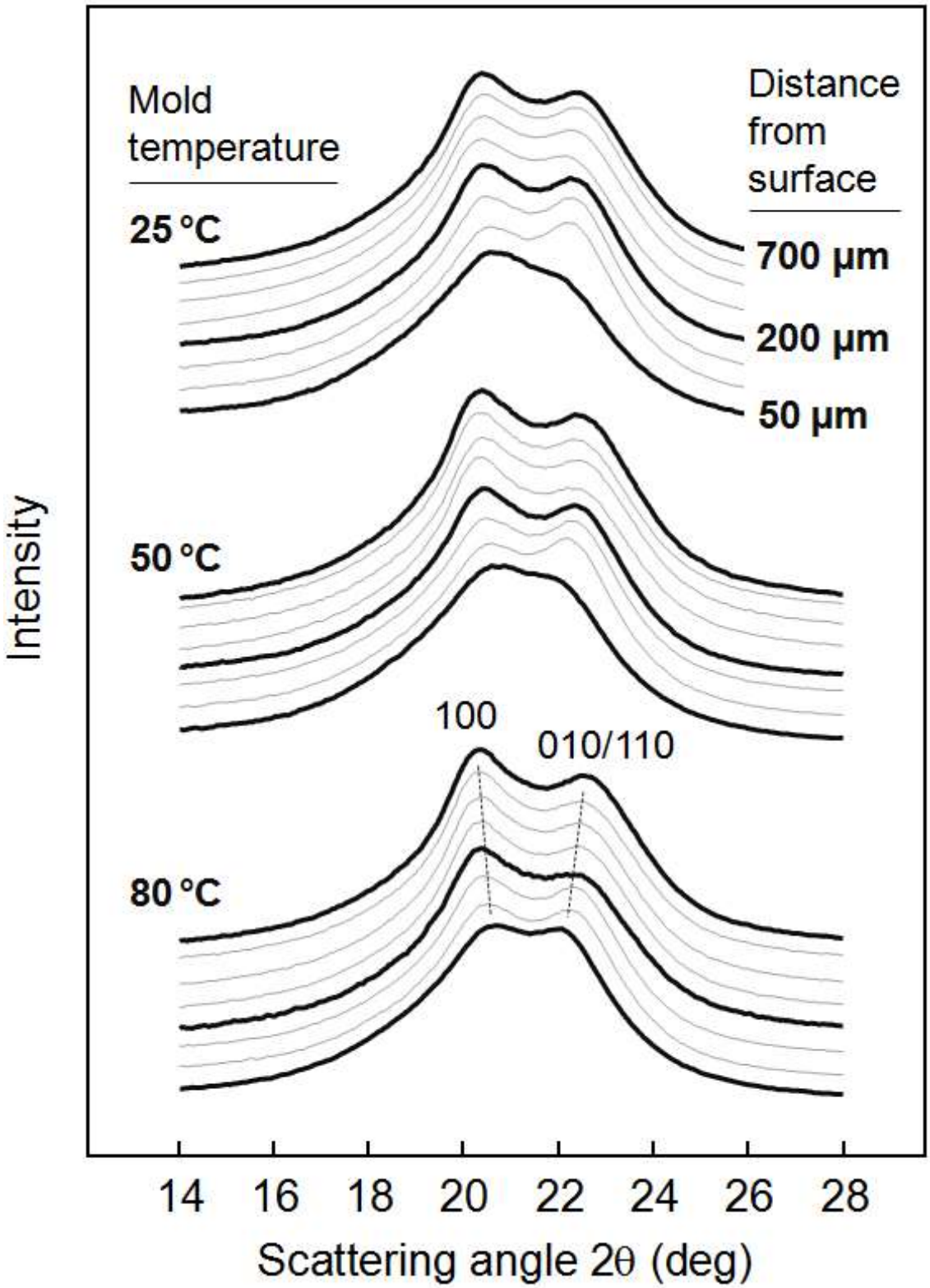

Figure 5: XRD patterns of specimens taken at different distance from the surface between 50 and 700 µm from PA 11 injection moldings prepared using different mold temperatures of 25 °C (top), 50 °C (center), and 80 °C (bottom).

Figure 6 shows two sets of XRD patterns redrawn from Figure 5 in order to demonstrate the effect of the mold-temperature on the structure of the skin (top set of curves) and core layers (bottom set of curves) in the injection moldings. It can be seen by the distance between 100 and 010/110 scattering peaks that in both the skin and core regions the perfection of the α-crystals improves with increasing mold temperature which, as discussed above, is related to an increase of the crystallization temperature.

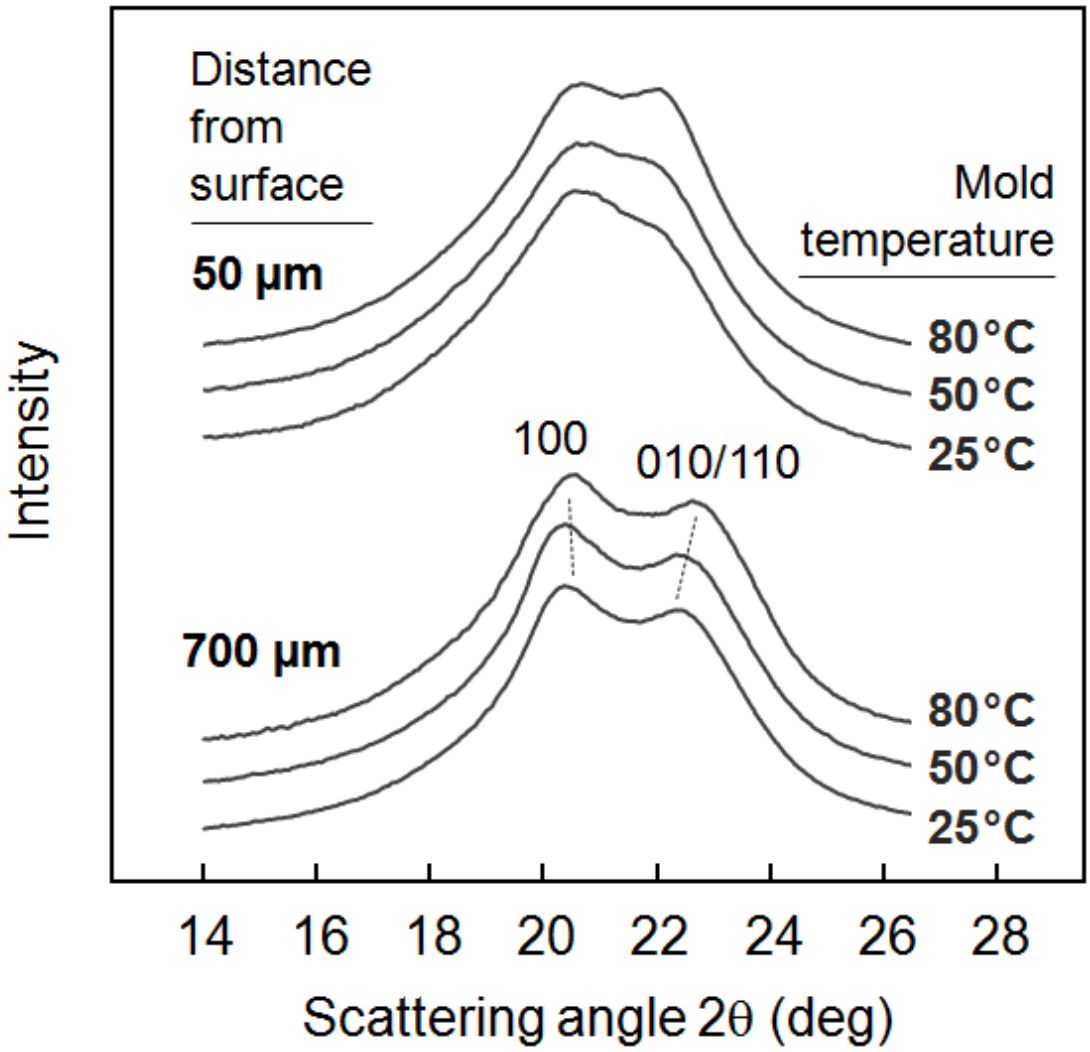

Figure 6: XRD patterns of specimens taken at different distance from the surface of 50 (top) and 700 µm (bottom) from PA 11 injection moldings prepared using different mold temperatures of 25 °C, 50 °C, and 80 °C.

Recently, the α-crystal/δ'-mesophase polymorphism of PA 11 including the perfection of α-crystals has been correlated with the temperature of isothermal melt-crystallization [14]. The crystallization that occurs during injection molding is influenced by shear-induced molecular orientation, and occurs at a cooling rate that slows as the material approaches the temperature of the steel mold. Crystallization nucleation undoubtedly occurs at a higher

temperature due to flow-induced effects, and subsequent crystal growth will occur during the cooling process, so the kinetic situation is complex. Nonetheless, it is hypothesized that the majority of crystal growth will occur within a narrow temperature range that will correlate closely to a discreet isothermal temperature and the resulting microstructure will have also an isothermal crystallization analog. In short, using fast scanning chip calorimetry, samples were cooled at a rate of 1000 K s^{-1} to different crystallization temperatures between 60 and 180 °C, with such high cooling rate assuring absence of crystallization before beginning the systematic isothermal crystallization experiments. After crystallization, the samples were cooled to room temperature at an identical rate of 1000 K s^{-1} and analyzed regarding the X-ray structure. This experimental route, designed to establish a relation between the crystallization temperature and the phase structure, was used to enhance the prediction of crystallization temperatures and ultimate phase structure in the injection moldings in the present study. In detail, such proof of (a) the reliability of the simulation of cooling rates in injection moldings and (b) the approach of predicting phase structures in the various layers below the surface by suggesting cooling-rate dependent crystallization temperatures obtained in independent non-isothermal crystallization experiments is done by comparison of the XRD pattern/phase structure obtained on isothermally crystallized PA 11 with the XRD pattern obtained from specimens taken at different distance from the surface of the injection moldings. The data in Figure 4 show both the expected variable cooling rate at distinct locations within the molded part, as obtained by simulation as well as the cooling rate dependent crystallization data obtained from fast scanning calorimetry data. Both pieces of information are required to estimate the crystallization conditions at specific depth locations in the molded part. From this data a relevant range of isothermal crystallization temperatures were determined. The data presented in Figure 7 shows a logical experimental relationship between the crystallization in the skin layer, approximately 50 μm below the surface of the molded sample and the sample created in the isothermal calorimetry studies. The XRD characterization of the molded sample most closely resembles the isothermal samples formed at 130°C suggesting that, during molding, crystallization occurs at temperatures around 120 to 130 °C. Similarly, the XRD data obtained from the core of the molded sample closely align with a higher-temperature isothermal sample. Therefore, for the core it is expected that crystallization may proceed at slightly higher temperatures between 130 to 140 °C. At the core of the sample, the accelerating influence of flow-induced crystallization is small, due to the fountain-flow shear profile through the thickness.

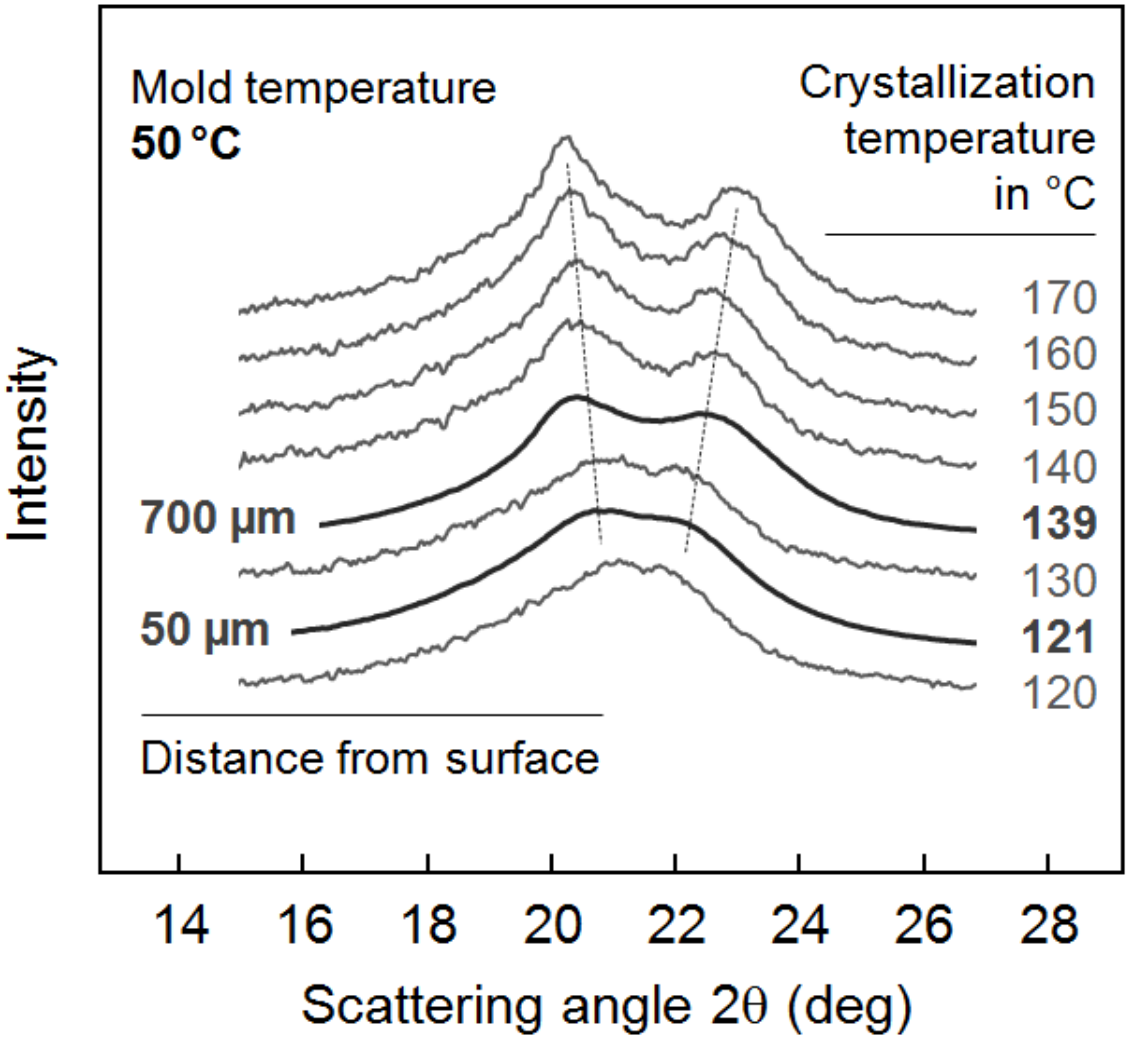

Figure 7: XRD patterns of specimens taken at different distance from the surface of 50 µm and 700 µm from a PA 11 injection molding prepared using a mold temperature of 50 °C, and samples isothermally crystallized from the relaxed melt at temperatures between 120 and 170 °C. The latter data were adapted from Polymer, Vol. 106, Rhoades AM, Wonderling N, Schick C, Androsch R, Supercooling-controlled heterogeneous and homogenous crystal nucleation of polyamide 11 and its effect onto the crystal/mesophase polymorphism, pages 29–34, Copyright (2016), with permission from Elsevier.

Figure 7 depicts the XRD patterns obtained from these regions of the injection molding prepared using a mold temperature of 50 °C with bold drawn black curves~~, respectively~~. The gray curves represent samples that were isothermally crystallized at the temperatures indicated at the right-hand side of the plot. First of all, it can be seen that with increasing crystallization temperature the perfection of the α-crystals improves, as judged by the angular position of the scattering peaks (see dash lines). However, more important is the observation of rather close similarity of the X-ray curves obtained from the specimens taken from the injection molding with predicted crystallization temperatures of 139 °C and 121 °C and X-ray curves obtained on samples isothermally crystallized at similar temperature. These similarities confirm the validity of the presented method; for PA 11 it

is possible to predict the α-crystal/δ'-mesophase polymorphism in the injecting moldings as well as degree of perfection of the α-crystals. It may be noted that the data obtained on thin sections of injection moldings in the present work, and data reported in [14] were acquired on FSC samples of a different PA 11 formulation and using a different experimental setup, not permitting a quantitative but only a qualitative comparison. This notwithstanding, the many simplifications of *e.g.* neglecting shear-induced crystallization effects or non-linear cooling rate profiles in injection molding are, at least for the specific processing conditions and material investigated here, of reduced importance.

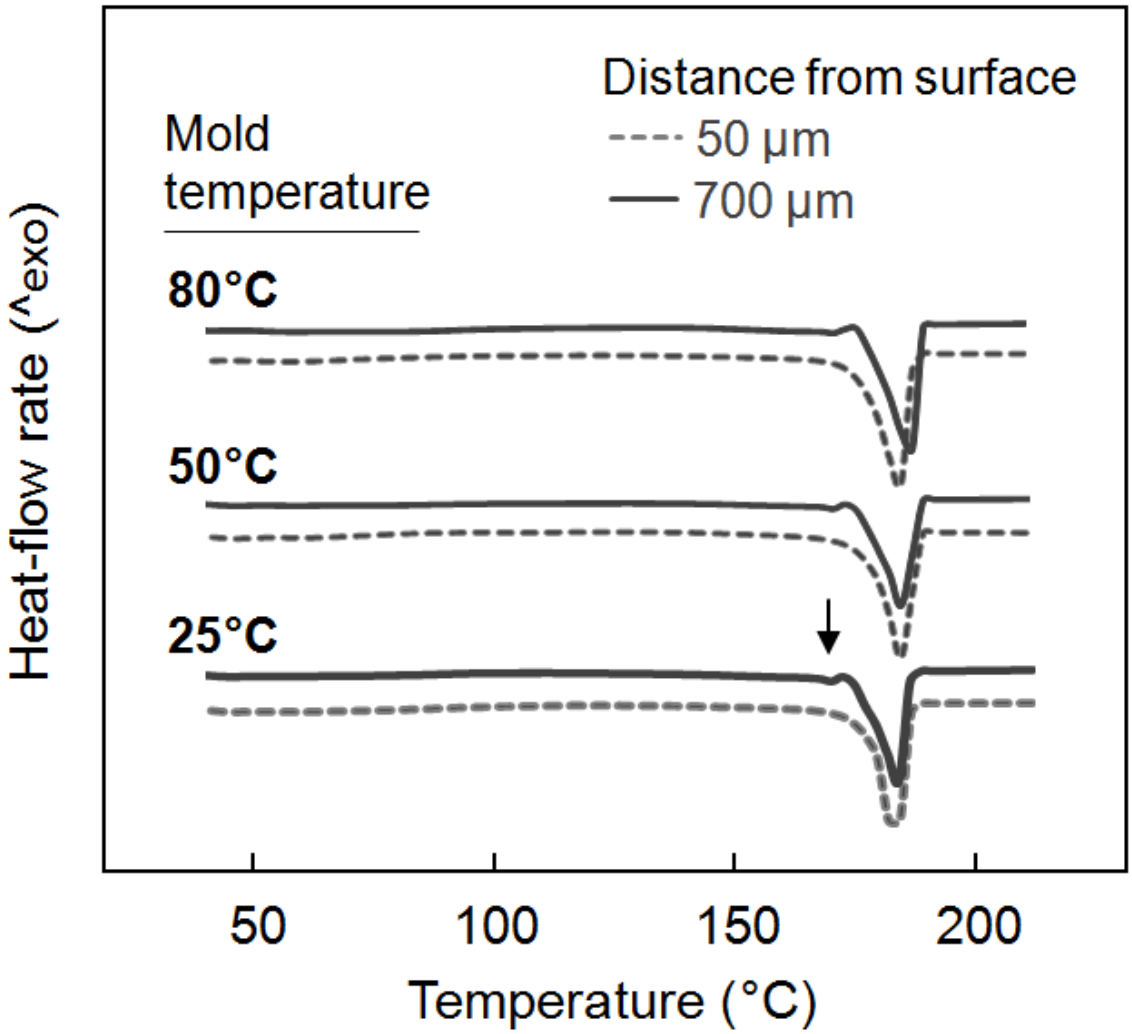

Figure 8: DSC heating scans obtained on samples taken from the skin and the core of PA 11 injection moldings prepared using mold temperatures of 25 °C (bottom), 50 °C (center), and 80 °C (top).

Figure 8 shows three sets of DSC scans obtained from the PA 11 injection moldings prepared at different mold temperatures of 25 °C (bottom), 50 °C (center), and 80 °C (top). The solid and dashed curves represent data observed on samples taken from the skin and core layers, respectively, with the sampling method illustrated in Figure 3. Most important,

regardless the mold temperature, the DSC data reveal presence of similar amount of crystals in both the skin and core layers of the molding. The crystallinity was estimated from the area of the observed melting peaks using a bulk enthalpy of melting of 189 J g^{-1} for normalization [39]. Accordingly, the crystallinity is around 25 % with negligible differences between skin and core, as well as negligible effect of the mold temperature. Reproducibly there has been observed a tiny pre-melting peak for samples taken from the core (see arrow). A possible reason is onset of melting in the core region at slightly lower temperature than in the skin, followed/superimposed by recrystallization at the selected slow-heating conditions [43–48]. This observation may point to slightly higher thermal stability of crystals in the skin. Despite XRD data have shown that crystals in the skin are more imperfect than in the core such higher stability may be attributed to the shear-induced orientation of the surrounding melt, that is, by reduced entropy of melting [49].

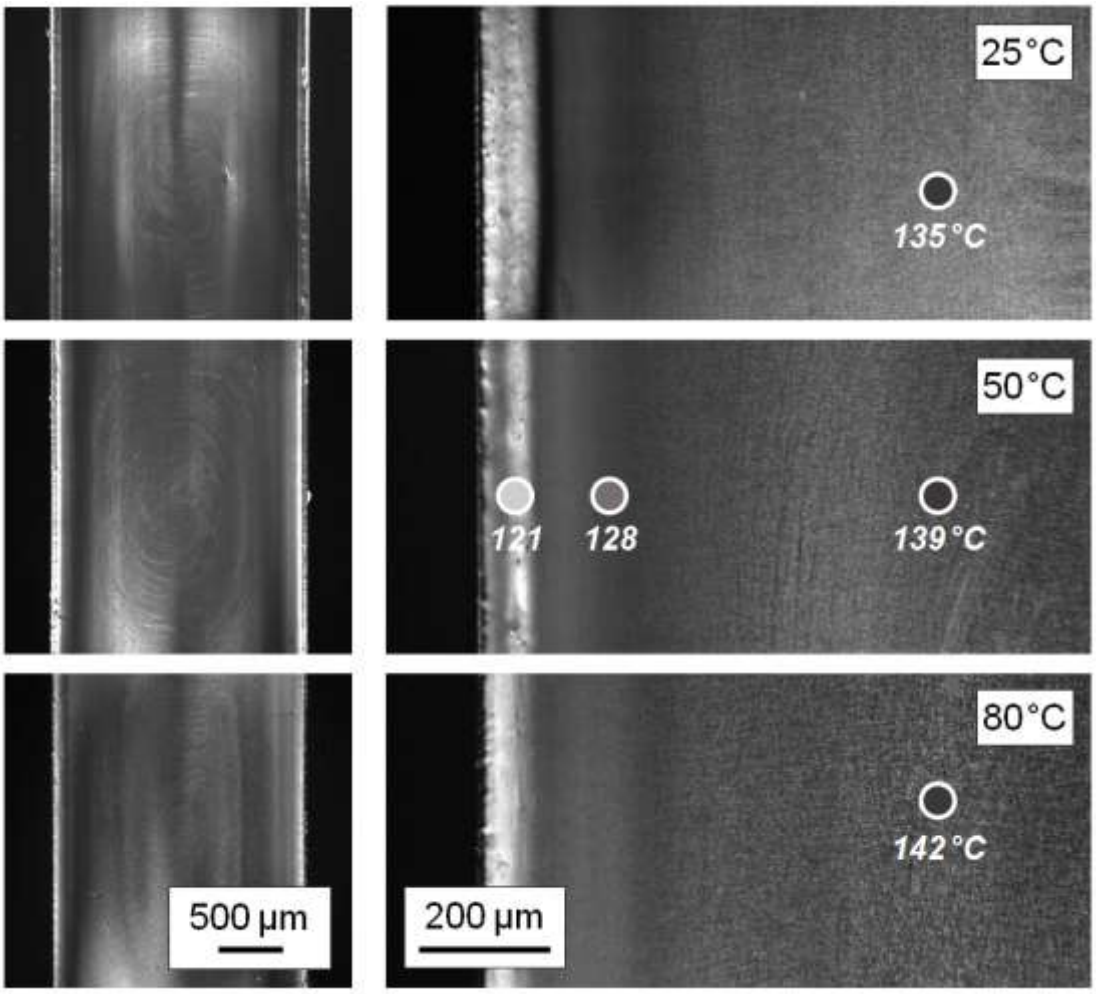

Figure 9: POM micrographs of the skin/core structures of PA 11 prepared using mold temperatures of 25 °C (top), 50 °C (center), and 80 °C (bottom). The complete cross-section is shown to the left while higher-magnification images are shown to the right. The circles in the center micrograph illustrate distances of 50, 200, and 700 µm from the surface of the sample, respectively, used for simulating the cooling rates in Figure 4; in addition, there is provided information about predicted crystallization temperatures.

Figure 9 shows POM micrographs of the complete cross-section (left) and of the cross-section near the surface at higher magnification (right) of the injection moldings processed using mold temperatures of 25 °C (top), 50 °C (center), and 80 °C (bottom). The circles in the center micrograph serve for illustration of the distance of the sampling locations of 50, 200, and 700 µm below the surface, respectively, used for simulating the cooling rates and prediction of the crystallization temperatures (see also Figure 4), including information about predicted crystallization temperatures. For all injection moldings, the micrographs which show the complete cross-section reveal that there is no shrinkage of the injection molded specimens during the solidification of the melt in the mold. At higher magnification, the skin layer reveals a non-spherulitic structure, which, however, gradually increases in thickness with decreasing mold temperature. In case of the sample processed using a mold temperature of 25 °C, the skin layer has a thickness of about 100 µm, while the thickness is only about 70 and 50 µm in case of mold temperatures of 50 and 80 °C, respectively.

The whitish appearing skin layer in the micrographs of Figure 9 is then followed by a featureless transition layer between the non-spherulitic skin and the fine-spherulitic central part of the moldings. This intermediate layer with a thickness of around 100–200 µm is interpreted as shear zone, which typically forms during injection molding due to the interaction of the immediately freezing skin layer when getting in contact with the cold mold-surface and still flowing melt during packing. It appears that the shear zone is reduced in thickness in case of an increased mold temperature.

Regarding the core region, a fine-spherulitic structure is observed in all samples with only small differences detected with respect to spherulite size. Figure 10 shows micrographs of the core region of the injection molding prepared using mold temperatures of 25 °C (left), 50 °C (center), and 80 °C (right) at larger magnification, revealing that the spherulite size marginally increases with the temperature of the mold. This result is expected as the density of crystal nuclei typically increases with decreasing temperature leading to larger spherulites. Note that at a distance of 700 µm below the surface, the data in Figure 4 suggest crystallization temperatures of 135, 139, and 142 °C when injection molding PA 11 using mold temperatures of 25, 50, and 80 °C, respectively.

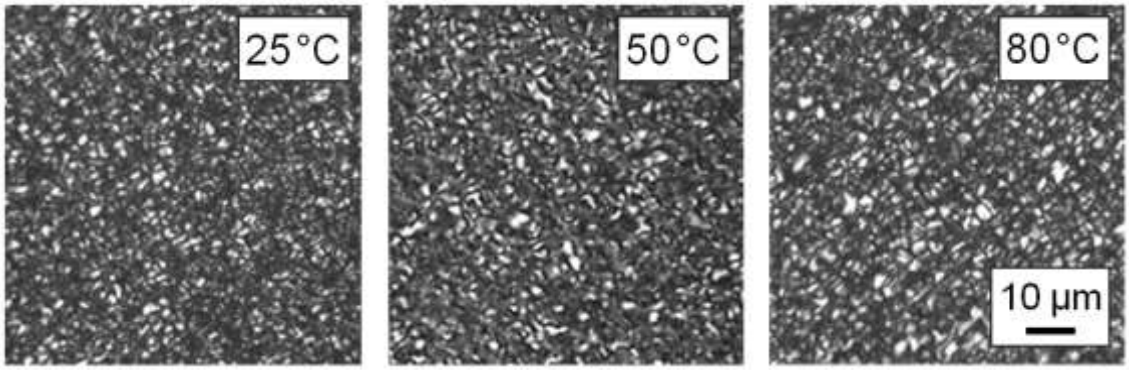

Figure 10: POM micrographs of the core region of PA 11 prepared using mold temperatures of 25 °C (left), 50 °C (center), and 80 °C (right).

Conclusions

The skin/core structure and semicrystalline morphology of injection molded PA 11 was investigated by X-ray diffraction (XRD), polarized-light optical microscopy (POM), and differential scanning calorimetry (DSC). The skin layer and shear zone appeared featureless in POM, while in the core region spherulitic crystallization was detected. DSC, however, revealed a similar crystal fraction of around 25 % in both skin and core. XRD, in addition, allowed identification of presence of α-crystals with their perfection increasing from skin to core. Near the surface, these α-crystals were extremely imperfect with a structure close to that of the pseudo-hexagonal γ-mesophase.

A concept of prediction of the structure of injection moldings has been introduced and validated. It includes simulation of the cooling-rate profile in all regions of the molding as a function of the temperature of the melt, and forecasting the corresponding temperatures of crystallization, based on non-isothermal quiescent-melt crystallization experiments performed independently. It appears by observation of similar semicrystalline morphologies in the various regions of the injection moldings with that in samples crystallized from the relaxed melt at comparable conditions that the suggested approach of predicting the structural gradient in injection moldings is reliable and does not necessarily need to account for shear-induced crystallization effects for this particular polymer.

Acknowledgments

Financial support by the Deutsche Forschungsgemeinschaft (DFG) (Grant AN 212/18) is greatly acknowledged. The authors are thankful to Nichole Wonderling (Materials Characterization Laboratory, Penn State) for assistance in X-ray data collection.

References

[1] Rilsan PA 11, Product information; http://www.rilsan.com/en/rilsan-pa11/pa11-product-information/, accessed: Nov, 2016.

[2] C. S. Brazel, S. L. Rosen, *Fundamental principles of polymeric materials*, John Wiley & Sons, New Jersey, USA **2012**.

[3] T. A. Osswald, G. Menges, *Materials Science of Polymers for Engineers*, Hanser, Munich, **2012**.

[4] A. M. Cunha, S. Fakirov, *Structure Development During Polymer Processing*, Springer, Netherlands, **2000**.

[5] P. C. Painter, M. M. Coleman, *Essentials of Polymer Science and Engineering*, DEStech Publications, Lancaster, **2009**.

[6] R. Aelion, *Annali di Chimica Applicata* **1948**, *3*, 5.

[7] K. G. Kim, B. A. Newman, J. I. Scheinbeim, *J. Polym. Sci. Polym. Phys.* **1985**, *23*, 2477.

[8] P. K. Chen, B. A. Newman, J. I. Scheinbeim, K. D. Pae, *J. Mater. Sci.* **1985**, *20*, 1753.

[9] B. A. Newman, T. P. Sham, K. D. Pae, *J. Appl. Phys.* **1977**, *48*, 4092.

[10] S. Gogolewski, *Colloid Polym. Sci*. **1979**, *257*, 811.

[11] Q. Zhang, Z. Mo, H. Zhang, S. Liu, S. Z. D. Cheng, *Polymer* **2001**, *42*, 5543.

[12] S. S. Nair, C. Ramesh, K. Tashiro, *Macromol. Symp*. **2006**, *242*, 216.

[13] L. J. Mathias, D. G. Powell, J. P. Autran, R. S. Porter, *Macromolecules* **1990**, *23*, 963.

[14] A. M. Rhoades, N. Wonderling, C. Schick, R. Androsch, *Polymer* **2016**, *106*, 29.

[15] R. Brill, *J. Prakt. Chem.* **1942**, *161*, 49.

[16] G. F. Schmidt, H. A. Stuart, *Z. Naturforsch.* **1958**, *13*, 222.

[17] T. Sasaki, *Polym. Letters* **1965**, *3*, 557.

[18] A. Kawaguchi, T. Ikawa, Y. Fujiwara, M. Tabuchi, K. Monobe, *J. Macromol. Sci., Part B* **1981**, *20*, 1.

[19] A. Mollova, R. Androsch, D. Mileva, C. Schick, A. Benhamida, *Macromolecules* **2013**, *46*, 828.

[20] K. Jariyavidyanont, W. Focke, R. Androsch, *Colloid Polym. Sci.* **2016**, *294*, 1391.

[21] A. Rhoades, J. L. Williams, N. Wonderling, R. Androsch, J. Guo, *J. Therm. Anal. Cal.* **2017**, *127*, 939.

[22] A. N. Wilkinson, A. J. Ryan, *Polymer processing and structure development*, Kluwer Academic Publishers, Dordrecht, Netherlands, **1998**.

[23] A. Sorrentino, F. De Santis, G. Titomanlio, in *Progress in understanding of polymer crystallization*, (Eds: G. Reiter, G. R. Strobl), Springer, Berlin Heidelberg, **2007**, p. 329.

[24] R. Androsch, C. Schick, *Adv. Polym. Sci.* **2017**, *276*, 1391.

[25] A. Toda, R. Androsch, C. Schick, *Polymer* **2016**, *91*, 239.

[26] C. Schick, R. Androsch, in *Fast scanning calorimetry* (Eds: C. Schick, V. B. F. Mathot), Springer, Switzerland **2016**, p. 463.

[27] S. S. Katti, J. M. Schultz, *Polym. Eng. Sci.* **1982**, *22*, 1001.

[28] D. P. Russell, P. W. R. Beaumont, *J. Mater. Sci.* **1980**, *15*, 197.

[29] D. Drummer, S. Meister, *Int. J. Polym. Sci.* **2014**, Article ID 718926, 8 pages.

[30] J. W. Housmans, M. Gahleitner, G. W. M. Peters, H. E. H. Meijer, *Polymer* **2009**, *50*, 2304.

[31] M. R. Kantz, H. D. Newman, F. H. Stigale, *J. App. Polym. Sci.* **1972**, *16*, 1249.

[32] R. Čermák, M. Obadal, P. Ponížil, M. Polášková, K. Stoklasa, A. Lengálová, *Eur. Polym. J.* **2005**, *41*, 1838.

[33] T. D. Fornes, D. R. Paul, *Polymer* **2003**, *44*, 3945.

[34] N. S. Murthy, V. A. Kagan, R. G. Bray, *Polym. Eng. Sci.* **2002**, *42*, 940.

[35] S. Apichartpattanasiri, J. N. Hay, S. N. Kukureka, *Wear* **2001**, *251*, 1557.

[36] B. Yalcin, D. Valladares, M. Cakmak, *Polymer* **2003**, *44*, 6913.

[37] L. Shen, I.Y. Phang, T. Liu, *Polym. Testing* **2006**, *25*, 249.

[38] I. Kolesov, D. Mileva, R. Androsch, *Polym. Bull.* **2014**, *711*, 581.

[39] Q. Zhang, Z. Mo, S. Liu, H. Zhang, *Macromolecules* **2000**, *33*, 5999.

[40] S. S. Nair, C. Ramesh, K. Tashiro, *Macromolecules* **2006**, *39*, 2841.

[41] M. Hirami, *J. Macromol. Sci., Phys.* **1984**, *B23*, 397.

[42] R. Androsch, M. Stolp, H. J Radusch, *Acta Polym.* **1996**, *47*, 99.

[43] A. A. Minakov, D. A. Mordvintsev, C. Schick, *Polymer* **2004**, *45*, 3755.

[44] A. A. Minakov, D. A. Mordvintsev, R. Tol, C. Schick, *Thermochim. Acta* **2006**, *442*, 25.

[45] D. Mileva, R. Androsch, E. Zhuravlev, C. Schick, B. Wunderlich, *Polymer* **2011**, *52*, 1107.

[46] D. Mileva, R. Androsch, E. Zhuravlev, C. Schick, B. Wunderlich, *Thermochim. Acta* **2011**, *522*, 100.

[47] R. Androsch, E. Zhuravlev, C. Schick, *Polymer* **2014**, *55*, 4932.

[48] D. Mileva, R. Androsch, E. Zhuravlev, C. Schick, *Macromolecules* **2009**, *42*, 7275.

[49] B. Wunderlich, Macromolecular Physics, Volume 3, Crystal melting, Academic Press, New York, **1980**, page 129.